Original Article

Prediction of hemorrhagic transformation after experimental ischemic stroke using MRI-based algorithms

Mark JRJ Bouts[1,2,3,4], Ivo ACW Tiebosch[1],
Umesh S Rudrapatna[1], Annette van der Toorn[1],
Ona Wu[2] and Rick M Dijkhuizen[1]

Abstract

Estimation of hemorrhagic transformation (HT) risk is crucial for treatment decision–making after acute ischemic stroke. We aimed to determine the accuracy of multiparametric MRI-based predictive algorithms in calculating probability of HT after stroke. Spontaneously, hypertensive rats were subjected to embolic stroke and, after 3 h treated with tissue plasminogen activator (Group I: n = 6) or vehicle (Group II: n = 7). Brain MRI measurements of T_2, $T_2{}^*$, diffusion, perfusion, and blood–brain barrier permeability were obtained at 2, 24, and 168 h post-stroke. Generalized linear model and random forest (RF) predictive algorithms were developed to calculate the probability of HT and infarction from acute MRI data. Validation against seven-day outcome on MRI and histology revealed that highest accuracy of hemorrhage prediction was achieved with a RF-based model that included spatial brain features (Group I: area under the receiver-operating characteristic curve (AUC) = 0.85 ± 0.14; Group II: AUC = 0.89 ± 0.09), with significant improvement over perfusion- or permeability-based thresholding methods. However, overlap between predicted and actual tissue outcome was significantly lower for hemorrhage prediction models (maximum Dice's Similarity Index (DSI) = 0.20 ± 0.06) than for infarct prediction models (maximum DSI = 0.81 ± 0.06). Multiparametric MRI-based predictive algorithms enable early identification of post-ischemic tissue at risk of HT and may contribute to improved treatment decision-making after acute ischemic stroke.

Introduction

Despite its effectiveness in improving clinical outcome in acute ischemic stroke patients, application of thrombolytic therapy with tissue plasminogen activator (tPA) or by mechanical thrombectomy is limited by strict guidelines, because of increased risk of hemorrhagic transformation (HT) beyond the 4.5 or 6-h therapeutic time windows of tPA or thrombectomy, respectively.[1–3] Nevertheless, some patients may still benefit from thrombolysis even well beyond 4.5–6 h after stroke onset.[2,3] Individualized assessment criteria evaluating the risk of developing HT are therefore warranted for efficient inclusion or exclusion of patients for thrombolytic treatment.

Neuroimaging, and especially MRI, has shown to be effective in identifying tissue at risk of infarction.[4]

Additionally, diffusion- and perfusion-weighted MRI may inform on risk of HT. Substantial reduction in tissue water diffusion,[5] large initial lesion volume on

[1]Biomedical MR Imaging and Spectroscopy Group, Center for Image Sciences, University Medical Center Utrecht, Utrecht, The Netherlands
[2]Athinoula A Martinos Center for Biomedical Imaging, Massachusetts General Hospital, Charlestown, MA, USA
[3]Leiden Institute for Brain and Cognition, Institute of Psychology, Leiden University, Leiden, The Netherlands
[4]Department of Radiology, Leiden University Medical Center, Leiden, The Netherlands

Corresponding author:
Mark Bouts, Biomedical MR Imaging and Spectroscopy Group, Center for Image Sciences, Heidelberglaan 100, 3584CX, Utrecht, The Netherlands.
Email: markinvivonmr@gmail.com

diffusion-weighted MRI,[5,6] large area of perfusion loss,[7] and regions with very low cerebral blood volume (CBV)[8,9] have all been proposed as indicators of increased risk of HT. In addition, early parenchymal signal enhancement on T_1-weighted MR images after injection of gadolinium-containing contrast agent, indicative of increased blood-brain barrier (BBB) permeability, may provide an early sign of HT.[10–15] Nevertheless, as a single measure, none of these MRI-based indices has been shown to be able to reliably identify tissue at risk of HT prior to thrombolytic treatment.[8,12]

Voxel-wise algorithms that integrate different measures of ischemic pathophysiology may improve early identification of tissue likely to undergo HT. Previous studies have demonstrated that this approach effectively allows calculation of probability of infarction at a voxel level.[4] Yet, the potential of predictive algorithms to signify tissue at risk of HT has not been evaluated. Hence, this study aimed to determine the efficacy of advanced prediction algorithms based on multiple MRI parameters to estimate risk of HT in ischemic stroke following reperfusion. To that aim, probability of HT and infarction was calculated from acute multiparametric MRI after embolic ischemic stroke in spontaneously hypertensive rats, which we compared against follow-up tissue outcome after tPA or vehicle treatment.

Materials and methods

Animal model

Data involved retrospective analyses of stroke animals used for a blinded thrombolytic treatment study (unpublished data). All animal procedures were approved by the animal ethical and experimental care committee of the University Medical Center Utrecht and Utrecht University, followed the guidelines of the European Union's Council Directive, and were performed in accordance with the ARRIVE (Animal Research: Reporting *In Vivo* Experiments) guidelines. Male spontaneously hypertensive rats (280–330 g) were subjected to right-sided embolic middle cerebral artery occlusion (MCAo) as previously described.[16] In brief, rats were endotracheally intubated and mechanically ventilated with 2% isoflurane in air:O_2 (1:2). Animals received subcutaneous injections of gentamicin (5 mg/kg) as antibiotic, and 2.5 ml glucose solution (2.5% in saline) to prevent dehydration. During all procedures core temperature was kept at $37.5 \pm 0.5°C$ with a temperature-controlled heating pad. To induce thromboembolic stroke, the right carotid artery was exposed by a ventral incision in the neck and a modified catheter was advanced into the internal carotid artery towards the origin of the middle cerebral artery (MCA).[16,17] A homologous (25 mm long, 24-h old) blood clot was slowly injected followed by removal of the catheter. The wound was closed and animals were directly prepared for MRI (see below). After MCAo and the first MRI session, animals were immediately treated with an intravenous infusion of vehicle (n = 10, Group I) or 10 mg/kg tPA (Activase®; concentrated to 3 mg/ml) (n = 10, Group II), of which 10% was administered as a bolus, followed by continuous infusion of the remaining 90% over 30 min.

Postoperative care included subcutaneous injections (directly and 8 h post-surgery) of 0.03 mg/kg buprenorphine for pain relief (Temgesic®, Ricket & Colman, Kingston-Upon-Hill, UK) and glucose (2.5%) in 2.5 ml saline (directly and 24-h post-surgery). Animals were socially housed according to a 12-h lights-on lights-off protocol. During the three subsequent days after stroke, Ringer's lactate (0–1 ml, depending on amount of weight loss) was daily administered to compensate for excessive weight loss.

MRI of tissue status

MRI was conducted on a 4.7 T animal MR system (Agilent, Palo Alto, CA, USA). A 90 mm diameter in-house developed Helmholtz volume coil was used for radiofrequency excitation, and a 25 mm diameter inductively coupled surface coil for signal reception.

MR imaging was conducted immediately after MCA occlusion, and again at 1 – to determine (re)perfusion status – and seven days – to determine outcome – after stroke. During MRI, animals were restrained in a MR-compatible holder with earplugs and a tooth-holder, and continuously mechanically ventilated with 2% isoflurane in air:O_2 (2:1). Body temperature and expired CO_2 were monitored and kept within physiological range.

For all MRI acquisitions, the field-of-view (FOV) was fixed to $32 \times 32 mm^2$, with a slice thickness of 1 mm. The MRI protocol consisted of multiple spin-echo T_2-weighted images (repetition time (TR) 3600 ms; echo time (TE) 12–144 ms; data matrix size $256 \times 128 \times 19$) and multiple gradient-echo T_2*-weighted images (TR 1400 ms; TE 7–70 ms; data matrix size $256 \times 128 \times 19$) acquired for reconstruction of quantitative T_2 maps and T_2* maps by non-linear least square fitting using a Levenberg–Marquardt algorithm according to

$$S(TE) = S_0\left(e^{-TE/T_2(*)}\right)$$

with S_0 as the estimated proton density.[18] To ensure adequate fitting, we only included voxels with goodness of fit measures, expressed by R^2, equal or above 0.95 for further analysis.

Maps of the apparent diffusion coefficient (ADC) were acquired after fitting the full tensor of the diffusion matrix obtained by diffusion-weighted 8-shot echo planar imaging (EPI) (TR 3500 ms; TE 38.5 ms; b-values 0 and 1428 s/mm^2; six diffusion-weighted directions; data matrix size $128 \times 128 \times 19$).[18] Dynamic susceptibility contrast-enhanced (DSC) MRI was acquired using gradient echo EPI (TR 330 ms; TE 25 ms; data matrix size $64 \times 64 \times 5$) in combination with an intravenous bolus injection of 0.35 mmol/kg gadobutrol (Gadovist®, Schering, The Netherlands). Maps of CBF, CBV, mean transit time (MTT), and time-to-maximum contrast agent arrival (T_{max}) were subsequently acquired by circular deconvolution of the tissue concentration curves with an arterial reference curve obtained from the contralateral hemisphere.[19] T_1-weighted images (gradient echo; TR 160 ms; TE 4 ms; data matrix size $256 \times 128 \times 19$) were acquired to assess blood–brain barrier integrity. T_1-weighted images were acquired every 2.73 min from just before, up to 35 min after gadobutrol injection. T_1-weighted images were then used to calculate quantitative T_1 maps using

$$S(TR) = S_0 \left(1 - e^{-TR/T_1}\right) e^{-TE/T_2^*}$$

with S_0 as the estimated proton density obtained from the T_2 mapping routine, and T_2^* as calculated from the T_2^* mapping routine. To compensate for differences in gain and reconstruction settings of the T_1-weighted versus T_2- and T_2^*-weighted acquisitions, an extra scaling factor of 16.5 was used to achieve T_1 in normal ranges.[20] R_1 ($1/T_1$) maps were subsequently used for estimation of the blood-to-brain transfer constant (K_i) and distribution space of intravascular Gd-shifted protons (V_p) using the Patlak matrix analysis of compartmental dynamics with a plasma concentration estimate from the sagittal sinus (four voxels).[21,22]

Histological assessment of intracerebral hemorrhage

Immediately after the final MRI session, animals were sacrificed and brains were extracted for assessment of extravascular blood disposition and scoring of hemorrhage degree. Animals were intraperitoneally injected with an overdose of pentobarbital followed by intracardial perfusion with cooled saline. Brains were extracted, cooled, and cut in 2 mm slices. Subsequently, slices were placed in ice cold PBS and covered with a glass slide to allow for photography. Photographs were taken on a 1 mm grid, using a digital color camera (Moticam2300, Motic, Germany) attached to binocular microscope. Digital images were then transferred to a separate workstation for visual assessment of extravascular

blood disposition. Presence of hemorrhage was scored visually on five consecutive slices using a four-point scale based on presence of no hemorrhage (NH); punctuate petechial hemorrhage, i.e. small extravascular blood spots (HI-1); confluent petechial hemorrhage, i.e. several clustered extravascular blood spots or reddish parenchyma (HI-2); and parenchymal hematoma, i.e. clear parenchymal space occupying blood occupying blood mass (PH).[23]

Image processing and analysis

T_2, ADC, perfusion parameter, and BBB index maps were spatially aligned and normalized using non-linear registration as previously described.[24] Mean contralateral gray matter values were calculated from four consecutive slices after exclusion of signal from cerebrospinal fluid. Infarcted tissue on post-stroke day 7 was automatically identified as voxels with T_2 values at least two standard deviations (2σ) higher than mean contralateral gray matter values. Perfusion and BBB abnormalities at the acute stage were similarly identified on MTT and K_i maps, respectively. Abnormalities on ADC, CBV and CBF maps were defined as 2σ lower than mean contralateral gray matter values. Hemispheric lesion fractions were calculated by dividing the lesion volume by the volume of the ipsilateral hemisphere.[24]

Hemorrhagic areas, characterized by clear focal hypointense signal compared to surrounding ipsilateral and homologous contralateral brain tissue with normal signal intensity, were outlined by two experienced researchers (I.T.: >6 years of experience in neurobiology; R.D.: >20 years of experience in neuroimaging). Manual outlines were created on the third echo image of the in vivo T_2^*-weighted MRI dataset (which allowed most straightforward depiction of hemorrhages with distinguishable contrast). Post mortem histological data were used as reference to confirm presence of hemorrhage and to prevent inclusion of non-hemorrhage-related susceptibility artifacts.

Predictive modeling

MRI-based predictive algorithms can calculate, based on training data, an optimized set of rules that map a relation of samples from the acutely acquired images to a class that represents either ultimately affected tissue or a class that represents non-affected tissue. Subsequently, this set of rules can be used to estimate the probability of pathology (e.g. HT or infarction) ($P_{outcome} = P(outcome | x_1,..,x_m)$) from newly introduced samples. Here, tissue outcome was predicted using statistical algorithms that relate acutely acquired normalized MRI parameters ($x = \{rT_2, rADC, rCBF, rCBV,$

rMTT, rT_{max}, rK_i, rV_p}) and possibly additional positional properties, i.e. the predictive features, to corresponding ultimate tissue status on follow-up MRI.

The features of the training sets were presented to a previously introduced parametric generalized linear model (GLM)[25] and a non-parametric random forest (RF) algorithm to estimate the probability of tissue injury at follow-up ($P_{outcome}$).[24] GLM calculates the probability of tissue injury using a logistic function:

$$P_{outcome} = \frac{1}{1 + e^{-\eta(x)}}$$

in which $\eta(x)$ is a linear link function that defines the relationship of M MRI parameters to tissue outcome at follow-up

$$\eta(x) = \sum_{j=1}^{M} \beta_{j^T} x_j + \alpha$$

in which β describes the weights of each MRI parameter, and α the bias or intercept of the linear function. Coefficients α and β can be estimated using an iterative reweighted least squares fitting.[25] RF is an ensemble algorithm that generates an aggregate result based on the predictions of multiple predictive algorithms. RF is a bootstrap aggregating approach in which multiple classification and regression trees (CART) are created by a randomized tree-building algorithm. During training, decision trees are grown from equally sized but modified subsets of the original training dataset. Further classification robustness is achieved by considering only a random subsample of the total available predictive features for node splitting. This also provides feature importance calculation, i.e. ranking features in their degree of contribution to the prediction. The aggregate result of the algorithm is achieved by normalized majority vote over the multiple decision trees. Further details on RF and feature importance calculation can be found elsewhere.[26]

Details on operational parameter optimization of the algorithms can be found in the Supplementary data.

To evaluate the accuracy of calculating the probability of HT or infarction acutely post-stroke, various training sets were used to develop the different types of predictive algorithms. For HT prediction, we created a training set containing data from tPA-treated spontaneously hypertensive rats (Group II), which are prone to develop hemorrhage. GLM- and RF-based algorithms were trained using acute multiparametric MRI compared against regions of intracerebral hemorrhage on post-stroke day 7 T_2*-weighted images to create a hemorrhage prediction model (hemorrhage prediction models A and B, respectively). To determine

improvement of prediction accuracy, training sets of algorithms similar to hemorrhage prediction models A and B were extended with additional spatial informative features of the brain (hemorrhage prediction models C and D; Figure 1).

To evaluate the accuracy of the hemorrhage predictive algorithms, both treatment groups were used to compare the estimated HT probability to the T_2*-derived hemorrhage region. Evaluation in the training set (i.e. tPA-treated animals) was conducted using leave-one-out cross-validation. This procedure prevents
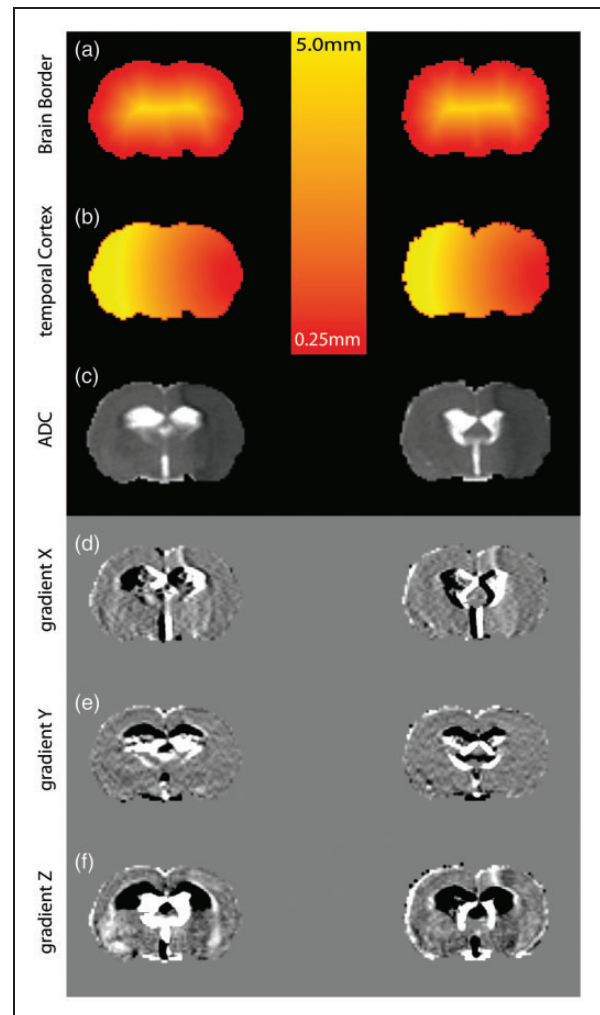

Figure 1. Depiction of spatial features included in hemorrhage prediction models C and D, and infarct prediction models A and B. Distance (in mm) to brain border (a), and distance to the ipsilateral temporal cortex (b) were used as positional features, effectively operating as penalty terms to reduce false positives in the contralateral hemisphere. Gradient images as derived from acute parametric maps (here for example ADC (c)) calculated along the x, y, and z direction (d, e and f, respectively) operated as extra contrast features.

prediction bias by repeatedly withholding one animal from the training set for evaluation while using the remaining animals for training.[4] Evaluations in the test group were based on an aggregate model calculated from the training group as a whole.

To determine whether the models' accuracy to predict HT was dependent on the underlying data or on the specific algorithm, we compared their performance with similar prediction models that were trained to predict infarction. Based on the best performing hemorrhage prediction model (i.e. Model D (see Results)), an RF-based infarct prediction model that included MRI parameters and spatial brain features was trained with data from vehicle-treated animals (i.e. Group I), representing unimpeded infarction development (infarct prediction model A). Since infarct volumes were much larger than hemorrhage volumes, we also tested the infarct prediction model with a restricted number of voxels; equaling the number of voxels (i.e. 1200) used in the hemorrhage prediction models (infarct prediction model B). Evaluation of infarct prediction performance was conducted similarly to that of the hemorrhage prediction models, except that Group I (i.e. vehicle-treated animals) was used for training, and infarction probabilities were compared against infarcted tissue measured on post-stroke day 7 T_2 maps.

For evaluation of prediction accuracy, probability maps were iteratively thresholded in step values of 1% ranging from 0 to 100%, and at each threshold, the voxels with correct and incorrect predictions of tissue pathology (i.e. hemorrhage or infarction) – true positives (TP) and false positives (FP), respectively – and absence of tissue pathology – true negatives (TN) and false negatives (FN), respectively – were calculated. This allowed calculation of model sensitivity

$$snc = \frac{TP}{TP + FN}$$

and specificity

$$spc = \frac{TN}{TN + FP}.$$

Subsequently, sensitivity and 1-specificity were used for receiver-operating characteristic (ROC) statistics. Quantitative comparisons were provided by calculating the area-under-the-curve of the ROC (AUC). At a fixed probability threshold of 50% (i.e. the likelihood of developing hemorrhage or infarction is more than 50%), the Youden's index (J) – defined as sensitivity + specificity − 1– was calculated to assess the overall performance of the algorithms in classifying affected tissue.[27] $J = 0$ indicates a low diagnostic value, whereas $J = 1$ indicates a perfect diagnosis. Dice's similarity

index (DSI)[24,28] was calculated to express the overlap of predicted hemorrhagic or infarcting tissue and tissue that actually hemorrhaged or infarcted at follow-up, defined as

$$DSI = \frac{2 * TP}{2 * TP + FP + FN}$$

The accuracy of the predicted values was assessed using the root mean square error defined as

$$RMSE = \frac{1}{N}\sqrt{\sum_{i=1}^{N}(y_i - p_i)^2}$$

in which N represents the total number of voxels, y_i the actual outcome at voxel I, and p_i the prediction. DSI, AUC, and J aim at maximizing values (towards 1), RMSE aims at minimizing values (towards 0). All predictive models and subsequent analysis were implemented and conducted in R (http://r-project.org).[29]

Data analysis and statistics

Predicted lesion volumes, expressed as volumetric fraction of the ipsilateral hemisphere (predicted hemispheric lesion fraction), were calculated from GLM- or RF-based estimation of probability of hemorrhage or infarction exceeding 50%.

ROC analysis was extended by thresholding of brain tissue with lowered CBV or ADC from 2σ up to 5σ (steps of 0.5σ) below mean contralateral values. Thresholded maps were subsequently summed and normalized by the number of thresholds used. Sensitivity and specificity, J, and DSI were calculated at the set threshold of 2σ. A similar strategy was applied for K_i with values above threshold (from 2σ from contralateral mean value).

MRI parameters and prediction performance measures were statistically analyzed with repeated measures ANOVA and post hoc false discovery rate (FDR) detection. Probability of hemorrhage or infarction was evaluated with a Wilcoxon rank sum test followed with post hoc FDR detection.

Results

Animal model

Out of 20 animals, two animals (Group I, n = 1; Group II, n = 1) developed subarachnoid hemorrhage and five animals (Group I, n = 2; Group II, n = 3) did not display cerebral hypoperfusion at the first MRI time-point. These animals were excluded from this study.

All but 3 (Group I, n=1; Group II, n=2) of the remaining 13 animals, showed signs of reperfusion, i.e. more than 40% increase in CBF from the acute to the 24-h time-point. At day 7, intracerebral hemorrhage was histologically scored as NH (Group I, n=1), HI-1 (Group I, n=4; Group II, n=3), HI-2 (Group II, n=2), or PH (Group I, n=2; Group II, n=1).

MRI of tissue status

Figure 2 shows maps of acute ADC, CBF, CBV, MTT, and K_i from rats prior to vehicle or tPA treatment. Follow-up imaging revealed infarcted tissue (as characterized by prolonged T_2) and hemorrhagic tissue (as characterized by reduced T_2*-weighted signal intensity). Acute tissue perfusion and diffusion indices in subsequently infarcted and hemorrhagic areas were significantly different from contralateral values, except for CBV in hemorrhagic regions (Supplementary Figure 1). K_i and V_p in infarcting or hemorrhagic areas were not statistically different from values in contralateral tissue. T_{max} was significantly longer in subsequently hemorrhagic areas than in infarcting areas.

Hemispheric hemorrhagic volume fractions were 0.04 ± 0.04 in Group I and 0.05 ± 0.02 in Group II, while hemispheric infarct volume fractions were 0.42 ± 0.10 (Group I) and 0.40 ± 0.10 (Group II), at seven days after stroke. Hemispheric volume fractions of acutely lowered CBV had similar sizes as subsequent hemorrhagic volumes (0.08 ± 0.11 (Group I) and 0.04 ± 0.04 (Group II)), whereas hemispheric volume fractions with elevated K_i or lowered ADC and CBF were somewhat larger (Group I: 0.14 ± 0.07 (K_i), 0.29 ± 0.14 (ADC) and 0.21 ± 0.19 (CBF); Group II:

0.15 ± 0.09 (K_i), 0.35 ± 0.13 (ADC) and 0.20 ± 0.12 (CBF)).

Predictive modeling – Hemorrhage

Thresholding of the volumes with abnormal ADC, CBV, and K_i revealed overlap with areas with subsequent HT (Figure 3). AUC, *J*, and sensitivity were highest for ADC-based thresholding (Table 1). However, CBV- and K_i-based thresholding resulted in highest specificity values. Voxel-wise hemorrhage prediction predictive models mostly improved prediction accuracies as compared to the thresholding approaches. Figure 3 shows that hemorrhage prediction models A and B – trained using MRI parameters from tPA-treated animals (Group II) – were able to identify tissue that subsequently hemorrhaged; however, GLM-based Model A also assigned increased probability values to contralateral regions without HT, which was also observed for the thresholding methods. Inclusion of spatial brain features in hemorrhage prediction models C and D improved specificity of hemorrhage predictions. However, only RF-based Model D demonstrated accurate ipsilateral specificity of predicted hemorrhagic area, which largely matched with actual intracerebral hemorrhage at follow-up. Table 1 shows that incorporation of spatial brain features in RF-based Model D resulted in increased AUC and reduced RMSE. Despite these high classification scores, actual overlap between the predicted hemorrhagic area and the area that truly hemorrhaged (expressed by DSI) was relatively low for all tested models.

Figure 4 shows how assigned local hemorrhagic probability values differ between regions with TP, FP, TN, FN for hemorrhage. Assessment of prediction
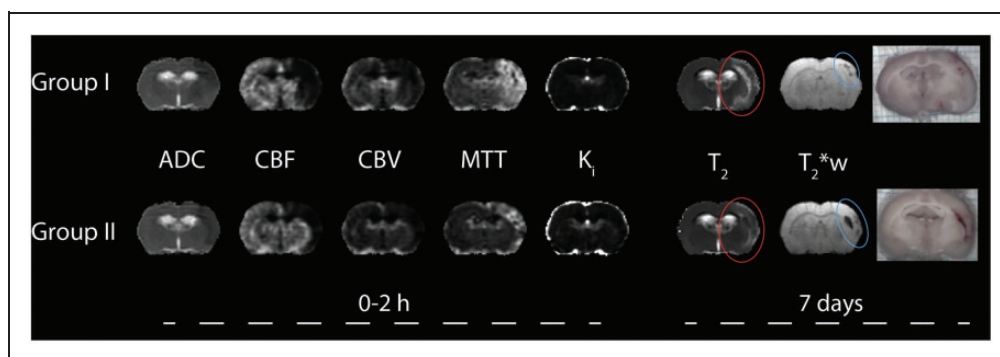

Figure 2. Images of coronal slices of a rat brain from the vehicle-treated (upper row) and tPA-treated group (lower row). Acute (2 h post-stroke; before treatment) maps of diffusion (ADC), perfusion (CBF, CBV and MTT), and BBB permeability (K_i) indicate tissue abnormality as a result of ischemia (lowered diffusion, reduced perfusion and occasionally increased BBB leakage). Follow-up MRI and histology after seven days displayed infarcted tissue (characterized by prolonged T_2) (red ellipses) and intracerebral hemorrhage (characterized by reduced T_2*-weighted signal intensity (blue ellipses), and parenchymal blood accumulation).
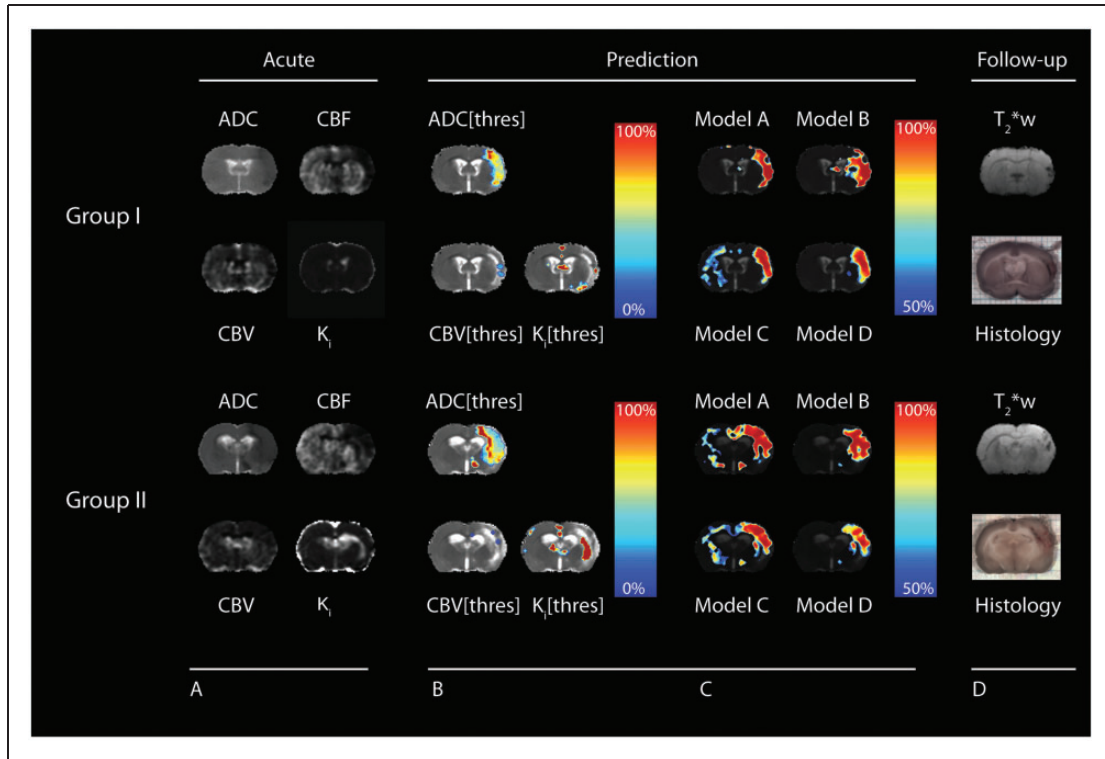
Figure 3. Maps of acute ADC, CBF, CBV, and K_i (panel A), with corresponding seven days post-stroke T_2*-weighted images and histological tissue sections (panel D) of vehicle- (Group I) and tPA-treated rats (Group II). Thresholded maps were voxel-wise summed and normalized between 0 and 100%, and overlaid on seven day follow-up T_2 maps (panel B). Thresholding of abnormal CBV showed most specific matching with subsequent hemorrhagic regions, as compared to K_i- and ADC-based thresholding. Of the predictive models, hemorrhage prediction model D (RF-based), which included MRI parameters as well as spatial brain features, demonstrated most optimal matching with ultimately hemorrhagic areas. Hemorrhagic probabilities above 50% are overlaid on seven day follow-up T_2 maps (panel C).

Table 1. Hemorrhage prediction accuracy for ADC, CBV, and K_i thresholding, and hemorrhage prediction models A–D.

Model	Group	AUC	J	Sensitivity	Specificity	DSI	RMSE
ADC(thres)	I	0.75 ± 0.11‡	0.51 ± 0.21	0.64 ± 0.24‡§	0.86 ± 0.05§	0.13 ± 0.07	N/A
	II	0.75 ± 0.11‡§	0.54 ± 0.11‡§	0.70 ± 0.12‡§	0.83 ± 0.09	0.18 ± 0.07	N/A
CBV(thres)	I	0.65 ± 0.14	0.29 ± 0.28	0.33 ± 0.31†	0.96 ± 0.05†	0.13 ± 0.12	N/A
	II	0.54 ± 0.06†	0.09 ± 0.11†	0.11 ± 0.12†	0.99 ± 0.01	0.11 ± 0.11	N/A
K_i(thres)	I	0.51 ± 0.03†	0.02 ± 0.07	0.11 ± 0.07†	0.92 ± 0.02	0.04 ± 0.04	N/A
	II	0.53 ± 0.07†	0.05 ± 0.14†	0.17 ± 0.20†	0.88 ± 0.07	0.05 ± 0.06	N/A
Model A	I	0.79 ± 0.16‡	0.47 ± 0.29	0.69 ± 0.32‡	0.78 ± 0.06‡§	0.11 ± 0.05	0.42 ± 0.06
	II	0.83 ± 0.07‡§	0.51 ± 0.12‡§	0.80 ± 0.21‡§	0.70 ± 0.11	0.18 ± 0.07	0.47 ± 0.10
Model B	I	0.77 ± 0.20	0.37 ± 0.29	0.67 ± 0.33‡	0.70 ± 0.08‡ + §‖	0.13 ± 0.05	0.45 ± 0.06
	II	0.83 ± 0.07‡†§‖	0.59 ± 0.08‡§	0.80 ± 0.18§	0.70 ± 0.14	0.20 ± 0.06*	0.44 ± 0.12
Model C	I	0.86 ± 0.08‡	0.51 ± 0.26	0.71 ± 0.30‡	0.80 ± 0.05‡§	0.10 ± 0.05	0.41 ± 0.05
	II	0.90 ± 0.02‡†§	0.65 ± 0.24§	0.86 ± 0.30‡§	0.78 ± 0.08	0.17 ± 0.06	0.42 ± 0.09
Model D	I	0.85 ± 0.14‡	0.53 ± 0.30	0.67 ± 0.35‡	0.86 ± 0.06	0.12 ± 0.05	0.36 ± 0.06
	II	0.89 ± 0.09‡†§	0.62 ± 0.24§	0.76 ± 0.32§	0.84 ± 0.09	0.19 ± 0.04*	0.36 ± 0.10

*$P < 0.05$ versus Group I; †$P < 0.05$ versus ADC(thres); ‡$P < 0.05$ versus K_i(thres); §$P < 0.05$ versus CBV(thres); ‖$P < 0.05$ versus model D; N/A: not applicable.

specificity demonstrated that probability values of TP regions were significantly increased over values in FN and TN regions for hemorrhage prediction models C and D. Significantly higher probability values in TP regions as compared to FP regions were observed in
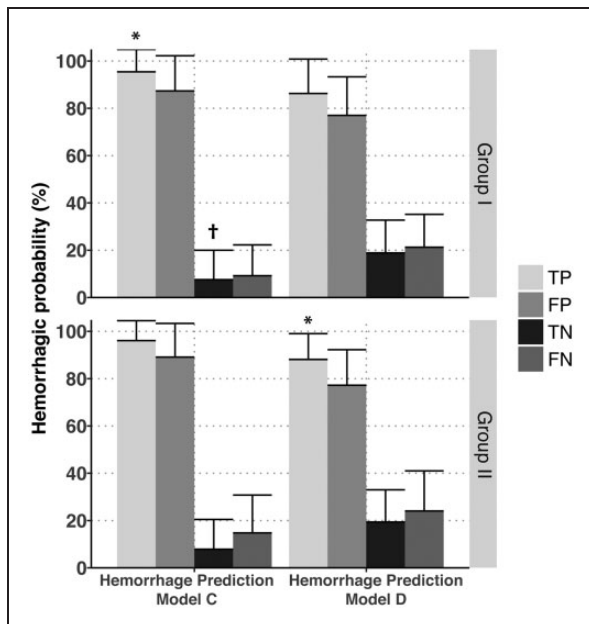

Figure 4. Assigned local hemorrhagic probability values of hemorrhage prediction models C and D in regions with TP, FP, TN, FN for hemorrhage in Group I and Group II rats (mean + standard deviation). Mean calculated hemorrhagic probability in TP regions was significantly higher than that in FP regions in Group I for hemorrhagic prediction model C and in Group II for hemorrhagic prediction model D, whereas mean hemorrhagic probability in TN regions was significantly lower in Model C-based predictions for Group I. *$P < 0.05$, TP versus FP. †$P < 0.05$, TN versus FN.

Group I for hemorrhage prediction model C ($P < 0.05$), and in Group II for hemorrhage prediction model D ($P < 0.05$). In Group I, probability values in TN regions were significantly different from probability values in FN regions for hemorrhage prediction model C ($P < 0.05$).

In the animal without follow-up hemorrhage, the area with acutely predicted HT was minor (Supplementary Figure 2). Model D-calculated hemorrhagic probability of the 50%-thresholded area in this animal was substantially lower than the mean probability in all other animals ($56 \pm 6\%$ vs. $75 \pm 6\%$, $P < 0.01$). Nevertheless, predictive models generally overestimated the tissue at risk of hemorrhage ($P < 0.05$ compared to ultimate hemorrhagic volume). Model D-based 50%-thresholded probability maps showed a smaller degree of overestimation (50%-thresholded volume fraction: Group I: 0.29 ± 0.12 ($P = 0.01$); Group II: 0.33 ± 0.17 ($P = 0.07$)) than Model C-based maps (Group I: 0.39 ± 0.08; Group II: 0.46 ± 0.15).

Predictive modeling – Infarction

Figure 5 shows examples of prediction of infarction in a vehicle-treated and a tPA-treated animal. Table 2 lists prediction accuracies measured for infarct prediction models A and B (trained using MRI parameters from vehicle-treated animals (Group I)). Both models were equally accurate in predicting infarction with significantly higher DSI values compared to the hemorrhage prediction models (Group I: $P < 0.01$; Group II: $P < 0.01$).

Discussion

We aimed to determine the accuracy of MRI-based voxel-wise predictive algorithms to identify tissue at
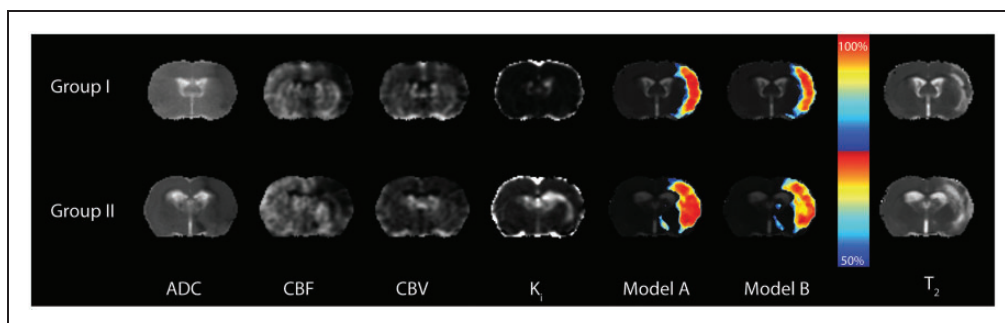

Figure 5. Maps of ADC, CBF, CBV, K_i, and calculated infarction probabilities (from Infarct Prediction Models A and B) in rat brain acutely after unilateral stroke, and follow-up T_2 map at day 7 for a vehicle- (Group I) and tPA-treated animal (Group II). Infarct prediction models (RF model based on MRI parameters and spatial features) were trained with inclusion of all infarcted voxels (Model A), or a reduced number of samples (i.e. 1200 voxels; Model B) comparable to the hemorrhage prediction models. The area of predicted infarction corresponded well with the actual ultimate infarct, with high similarity between the two models.

Table 2. Prediction accuracy measures for infarct prediction models A and B.

Model	Group	AUC	J	Sensitivity	Specificity	DSI	RMSE
Model A	I	0.94 ± 0.02	0.74 ± 0.09	0.84 ± 0.11	0.90 ± 0.02	0.81 ± 0.06	0.29 ± 0.02
	II	0.92 ± 0.08	0.70 ± 0.22	0.84 ± 0.11	0.87 ± 0.02	0.76 ± 0.18	0.31 ± 0.02
Model B	I	0.94 ± 0.02	0.73 ± 0.09	0.83 ± 0.22	0.90 ± 0.02	0.81 ± 0.06	0.31 ± 0.01
	II	0.91 ± 0.09	0.70 ± 0.23	0.84 ± 0.23	0.86 ± 0.02	0.75 ± 0.19	0.33 ± 0.02

risk of developing secondary hemorrhage after acute ischemic stroke. In an established animal model of stroke with reperfusion-induced HT, we found that individualized maps of hemorrhagic probability can be effectively obtained from a combination of MRI parameters, with highest accuracy when calculated with an RF-based supervised algorithm.

Assessment of the risk of HT in individual acute stroke patients may aid in pre-treatment decision-making and post-treatment monitoring to minimize detrimental effects of thrombolytic therapy. Earlier studies heralded the use of MRI as a potential tool for elucidating tissue at risk of hemorrhage. For example, very low CBV within the area of diffusion abnormality[8,9] or other voxel-wise combinations of abnormal ADC with T_{1sat}[30] have been associated with increased likelihood of hemorrhage after acute ischemic stroke. In these studies, viability thresholds were calculated to determine tissue outcome, subsequently generating discrete tissue theme maps depicting tissue at risk. Our study extends on these findings by: (1) including multiple (more than 2) MRI-based parameters of perfusion and tissue status, as well as spatial brain features; (2) ruling out assumptions on viability thresholds; and (3) calculating a probabilistic rather than discrete output.

Previously, supervised MRI-based prediction methods have been successfully employed to calculate probability of tissue infarction after acute clinical or experimental stroke.[4] In the current study, we used GLM- and RF-based predictive algorithms, and attained a high accuracy in predicting tissue infarction in a stroke model with spontaneously hypertensive animals. Importantly, reduction of the training data samples (i.e. image voxels) to a number comparable to the sample size in the hemorrhage prediction models did not significantly affect prediction accuracy. This reflects the potential of these models for the prediction of HT in cases where the size (i.e. voxel numbers) of available HT is substantially small. Although the accuracy of HT prediction was not as high as for infarction prediction, the multiparametric MRI-based algorithms improved the accuracy of prediction of HT regions over thresholding of single indices like K_i or CBV. Particularly for RF-based models, specificity of the prediction improved with inclusion of spatial brain features that

guided voxel-wise classification. This has also been observed in a study where spatial lesion distribution maps increased accuracy of prediction of tissue infarction.[31] However, infarct distribution depends on many factors, such as vascular occlusion site, type of occlusion, and duration of occlusion, which may be challenging to derive a priori in clinical practice. Therefore, we employed more general spatial features, such as distance from the brain border or distance from the temporal cortex, which can be unbiasedly derived from each individual subject.

Our results showed differences in distribution of probability values between GLM- and RF-based predictive algorithms. This may imply possibilities for risk-based differentiation of regions that will eventually hemorrhage versus those that may not, similar to what we have recently reported for multiparametric MRI-based infarct prediction models, where differences in assigned risk values may inform on tissue salvageability.[24] Yet, further experimentations are warranted to corroborate these observations. These studies should overcome the limitations of the current study and should include larger sample sizes (to minimize effects of individual variations) with sufficient differentiation between various hemorrhagic subtypes (including clinically relevant PH).

Despite the high prediction accuracies of our models, the actual overlap of the predicted hemorrhagic region and the region that actually hemorrhaged was relatively low. Although regions with predicted HT resided in close proximity to ultimately hemorrhagic areas (as reflected by measures of specificity and sensitivity), all tested prediction methods overestimated the tissue at risk of hemorrhage. Previous studies reported on a "compelling" correspondence between areas of projected HT and the actual hemorrhage, but did not effectually quantify the exact spatial correspondence.[8,9,11] Indefinite matching between early imaging markers and subsequent hemorrhagic development has also been observed by others, reporting an insignificant correspondence of early contrast-induced signal enhancement with subsequent HT.[32,33] Our study particularly focused on relatively gross hemorrhages identified as a local signal intensity reduction on T_2^*-weighted images, caused by the magnetic

susceptibility effect of deoxygenated blood, histologically verified from clear blood accumulation on post-mortem brain sections acquired directly after the final MRI session. Mild or microscopic hemorrhage may have remained undetected especially when obscured by edema-associated T_2 prolongation.[10]

The development of HT is strongly associated with increased permeability of the BBB.[34] MRI of early parenchymal enhancement as a result of leakage of contrast agent over the BBB has been shown to be predictive of development of HT in animal stroke models[10,11] and human stroke patients.[12–14] Yet in the current study, increased extravasation, reflected by elevated K_i, was only occasionally observed and was not necessarily associated with the hemorrhagic area. Our study aimed at identifying tissue likely to develop HT within a short, acute time-window of less than 3-h post-stroke, which may have been too early for progression of significantly elevated BBB permeability.[34] Furthermore, low perfusion, particularly in regions with severe CBV reductions (i.e. with increased risk of HT), may have restricted local contrast agent arrival despite potential presence of leaky vessels. Likewise, other studies have also reported limitations of the accuracy of BBB permeability measurements to predict successive hemorrhage.[11,32]

Although our study involved a relatively small sample size, our findings demonstrated an increased sensitivity in predicting areas at risk of post-stroke HT with voxel-wise multiparametric MRI-based prediction models as compared to single modality predictions. This further extends the potential of these models, which have been successfully applied to predict tissue at risk of infarction[4,24] and to identify tissue amenable for reperfusion therapy,[16,24] to inform on potential adverse effects of thrombolytic treatment after stroke. Whereas previous studies particularly focused on a single imaging marker for prediction of HT,[8,9,12–14,32] the current study employed computational models that combine information from multiple markers in a single probabilistic index. The resultant tissue theme maps may provide a straightforwardly interpretable alternative to manifold multifactorial images, with assigned index levels that make no assumptions on possible viability thresholds. Multiparametric MRI protocols, comparable to what we used in our preclinical study, are readily available on clinical scanners. Yet, requirement of multiple parameters in prediction models may imply a limitation for use within the time-critical phase of acute clinical stroke. However, technological developments that speed up acquisition and processing of multiparametric MRI data, for example by faster scanning protocols,[35] concurrent calculation of hemodynamic indices and BBB permeability from dynamic susceptibility contract-enhanced MRI,[36] or combined T_2 and ADC mapping from multi-echo diffusion-weighted imaging,[37] may facilitate use in clinical practice within the near future. Furthermore, improvements that enable differentiation between different hemorrhage subtypes, including symptomatic and asymptomatic intracerebral hemorrhage, would increase the diagnostic potential of prediction models. Clearly, further research is needed to establish the potential of these algorithms in clinical practice, where they may contribute assessments in which careful identification of presence and location of risk of hemorrhage can be critical for safe and effective intervention in acute ischemic stroke patients.

Declaration of conflicting interests

The author(s) declared no potential conflicts of interest with respect to the research, authorship, and/or publication of this article.

Authors' contributions

MJB participated in the experiments, analysis, and discussion of the results, manuscript preparation and the final revision; IAT participated in the experiments, manuscript preparation, and the final revision; USR participated in the experiments, discussion of the results, manuscript preparation and final revision; AT participated in the experiments, manuscript preparation and the final revision; OW participated in the discussion of the results, manuscript preparation, and the final revision; RMD participated in the analysis, and discussion of the results, manuscript preparation, and the final revision. All authors have read and approved the final manuscript.

Supplementary material

Supplementary material for this paper can be found at http://journals.sagepub.com/doi/suppl/10.1177/0271678X16683692

References

1. Hacke W, Kaste M, Bluhmki E, et al. Thrombolysis with alteplase 3 to 4.5 hours after acute ischemic stroke. *N Engl J Med* 2008; 359: 1317–1329.
2. Wardlaw JM, Murray V, Berge E, et al. Recombinant tissue plasminogen activator for acute ischaemic stroke: an updated systematic review and meta-analysis. *Lancet* 2012; 379: 2364–2372.

3. Mokin M, Rojas H and Levy EI. Randomized trials of endovascular therapy for stroke – impact on stroke care. *Nat Rev Neurol* 2016; 12: 86–94.

4. Wu O, Dijkhuizen RM and Sorensen AG. Multiparametric magnetic resonance imaging of brain disorders. *Top Magn Reson Imag* 2010; 21: 129–138.

5. Selim M, Fink JN, Kumar S, et al. Predictors of hemorrhagic transformation after intravenous recombinant tissue plasminogen activator prognostic value of the initial apparent diffusion coefficient and diffusion-weighted lesion volume. *Stroke* 2002; 33: 2047–2052.

6. Lansberg MG, Thijs VN, Bammer R, et al. Risk factors of symptomatic intracerebral hemorrhage after tPA therapy for acute stroke. *Stroke* 2007; 38: 2275–2278.

7. Albers GW, Thijs VN, Wechsler L, et al. Magnetic resonance imaging profiles predict clinical response to early reperfusion: the diffusion and perfusion imaging evaluation for understanding stroke evolution (DEFUSE) study. *Ann Neurol* 2006; 60: 508–517.

8. Alsop DC, Makovetskaya E, Kumar S, et al. Markedly reduced apparent blood volume on bolus contrast magnetic resonance imaging as a predictor of hemorrhage after thrombolytic therapy for acute ischemic stroke. *Stroke* 2005; 36: 746–750.

9. Campbell BCV, Christensen S, Butcher KS, et al. Regional very low cerebral blood volume predicts hemorrhagic transformation better than diffusion-weighted imaging bolume and thresholded apparent diffusion coefficient in acute ischemic stroke. *Stroke* 2010; 41: 82–88.

10. Dijkhuizen RM, Asahi M, Wu O, et al. Delayed rt-PA treatment in a rat embolic stroke model: diagnosis and prognosis of ischemic injury and hemorrhagic transformation with magnetic resonance imaging. *J Cereb Blood Flow Metab* 2001; 21: 964–971.

11. Neumann-Haefelin C, Brinker G, Uhlenküken U, et al. Prediction of hemorrhagic transformation after thrombolytic therapy of clot embolism: an MRI investigation in rat brain. *Stroke* 2002; 33: 1392–1398.

12. Kim EY, Na DG, Kim SS, et al. Prediction of hemorrhagic transformation in acute ischemic stroke: role of diffusion-weighted imaging and early parenchymal enhancement. *Am J Neuroradiol* 2005; 26: 1050–1055.

13. Hjort N, Wu O, Ashkanian M, et al. MRI detection of early blood-brain barrier disruption: Parenchymal enhancement predicts focal hemorrhagic transformation after thrombolysis. *Stroke* 2008; 39: 1025–1028.

14. Kastrup A, Gröschel K, Ringer TM, et al. Early disruption of the blood-brain barrier after thrombolytic therapy predicts hemorrhage in patients with acute stroke. *Stroke* 2008; 39: 2385–2387.

15. Warach S and Latour LL. Evidence of reperfusion injury, exacerbated by thrombolytic therapy, in human focal brain ischemia using a novel imaging marker of early blood–brain barrier disruption. *Stroke* 2004; 35: 2659–2661.

16. Tiebosch IACW, Crielaard BJ, Bouts MJRJ, et al. Combined treatment with recombinant tissue plasminogen activator and dexamethasone phosphate-containing liposomes improves neurological outcome and restricts lesion progression after embolic stroke in rats. *J Neurochem* 2012; 123(Suppl 2): 65–74.

17. Zhang RL, Chopp M, Zhang ZG, et al. A rat model of focal embolic cerebral ischemia. *Brain Res* 1997; 766: 83–92.

18. van der Zijden JP, van der Toorn A, van der Marel K, et al. Longitudinal in vivo MRI of alterations in perilesional tissue after transient ischemic stroke in rats. *Exp Neurol* 2008; 212: 207–212.

19. Wu O, Østergaard L, Weisskoff RM, et al. Tracer arrival timing-insensitive technique for estimating flow in MR perfusion-weighted imaging using singular value decomposition with a block-circulant deconvolution matrix. *Magn Reson Med* 2003; 50: 164–174.

20. Haacke EM, Brown RW, Thompson MR, et al. *Magnetic resonance imaging: physical principles and sequence design*, 1st ed. New York: Wiley-Liss, 1999.

21. Patlak CS and Blasberg RG. Graphical evaluation of blood-to-brain transfer constants from multiple-time uptake data. Generalizations. *J Cereb Blood Flow Metab* 1985; 5: 584–590.

22. Ewing JR, Knight RA, Nagaraja TN, et al. Patlak plots of Gd-DTPA MRI data yield blood–brain transfer constants concordant with those of 14C-sucrose in areas of blood–brain opening. *Magn Reson Med* 2003; 50: 283–292.

23. Henninger N, Bratane BT, Bastan B, et al. Normobaric hyperoxia and delayed tPA treatment in a rat embolic stroke model. *J Cereb Blood Flow Metab* 2009; 29: 119–129.

24. Bouts MJRJ, Tiebosch IACW, van der Toorn A, et al. Early identification of potentially salvageable tissue with MRI-based predictive algorithms after experimental ischemic stroke. *J Cereb Blood Flow Metab* 2013; 33: 1075–1082.

25. Wu O, Koroshetz WJ, Ostergaard L, et al. Predicting tissue outcome in acute human cerebral ischemia using combined diffusion- and perfusion-weighted MR imaging. *Stroke* 2001; 32: 933–942.

26. Breiman L. Random forests. *Machine Learn* 2001; 45: 5–32.

27. Wu O, Sumii T, Asahi M, et al. Infarct prediction and treatment assessment with MRI-based algorithms in experimental stroke models. *J Cereb Blood Flow Metab* 2007; 27: 196–204.

28. Dice LR. Measures of the amount of ecologic association between species. *Ecology* 1945; 26: 297–302.

29. R Core Team. *R: A language and environment for statistical computing. R Foundation for Statistical computing*. Vienna, Austria, 2015. Available at: https://www.R-project.org.

30. Ding G, Nagesh V, Jiang Q, et al. Early prediction of gross hemorrhagic transformation by noncontrast agent MRI cluster analysis after embolic stroke in rat. *Stroke* 2005; 36: 1247–1252.

31. Huang S, Shen Q and Duong TQ. Quantitative prediction of acute ischemic tissue fate using support vector machine. *Brain Res* 2011; 1405: 77–84.

32. Rozanski M, Ebinger M, Schmidt WU, et al. Hyperintense acute reperfusion marker on FLAIR is not associated with early haemorrhagic transformation in the elderly. *Eur Radiol* 2010; 20: 2990–2996.

33. Campbell BCV, Costello C, Christensen S, et al. Fluid-attenuated inversion recovery hyperintensity in acute ischemic stroke may not predict hemorrhagic transformation. *Cerebrovasc Dis* 2011; 32: 401–405.

34. Zoppo GJD, Kummer RV and Hamann GF. Ischaemic damage of brain microvessels: inherent risks for thrombolytic treatment in stroke. *J Neurol Neurosurg Psychiatry* 1998; 65: 1–9.

35. Nael K, Khan R, Choudhary G, et al. Six-minute magnetic resonance imaging protocol for evaluation of acute ischemic stroke: pushing the boundaries. *Stroke* 2014; 45: 1985–1991.

36. Skinner JT, Moots PL, Ayers GD, et al. On the use of DSC-MRI for measuring vascular permeability. *Am J Neuroradiol* 2016; 37: 80–87.

37. Nana R, Zhao T and Hu X. Single-shot Multi-echo parallel EPI for DTI with improved SNR and reduced distortion. *Magn Reson Med* 2008; 60: 1512–1517.